ESR and ENDOR Investigations of Radiation-Induced Metastable Paramagnetic Centers in CaWO₄[†]

Chihiro Kikuchi*

A review of a variety of paramagnetic centers in pure and doped CaWO₄, produced by gamma and neutron radiations is given. Gamma irradiation of samples containing Group V (V, Nb, Ta) elements produce ESR centers with $g > g_e$. It is suggested that these are hole centers. For the Group VI elements Cr and Mo, the g-values are less than g_e, suggesting that these are electron trapping centers. For W (Group VI), there are hole as well as electron trapping centers. The latter are particularly sensitive to the trivalent charge compensating ion. It is shown that two W centers and the Nb-center are responsible for the 155°, 225°, and 290°K thermoluminescent peaks in nominally pure CaWO₄ following gamma irradiation. Fast neutron irradiation results in three ESR centers, whose g-values along the c-axis are $g_\alpha = 2.005$, $g_\beta = 1.801$, and $g_\gamma = 1.746$. The γ-center is identified as a paramagnetic W associated with a nearest neighbor oxygen vacancy. Its concentration is in good agreement with Kinchin-Pease theory. The angular dependence of the β-center indicates that it is associated with a defect along the $\langle 110 \rangle$ directions. The identity of the α-center is not known. Other problems are pointed out.

I. INTRODUCTION

This report is intended as a sequel to the report[1] on the "Applications of Spin Resonance Techniques to the Study of Radiation Effects," in which some of the possible applications of electron spin resonance to radiation effects programs, such as the defect structure of MgO, ratio of gadolinium isotope thermal neutron capture cross sections, paramagnetic vanadium centers produced by gamma radiation, and others were discussed. Related programs have been developed in many other laboratories. One example is the detailed study of the defect structures of CaCO₃ by S. A. Marshall[2] and his associates, and another is the analysis of the spectra of Mn in NaCl by N. Itoh and his students at Nagoya University.[3] Although it was our hope to give a systematic review of these various programs, the project was abandoned because of the prohibitive amount of labor that would be required. Consequently, it was decided to limit the discussion in this paper to CaWO₄, concentrating mainly on the work at University of Michigan; we hoped in this way to prepare a "working" paper" to bring out some of the unsolved problems.

At the time our programs were started, there was considerable interest in

CaWO$_4$ as a host crystal for laser active rare-earth ions.[4] Very early it was found that considerable reduction in the laser threshold can be effected by co-doping the crystal with materials like Nb, in addition to the laser active Nd^{3+} center.[5] Thus there were questions about the nature of the charge-compensation mechanism. Another motivation was provided by the scintillation properties of CaWO$_4$. Studies by G. B. Beard, W. H. Kelly, and M. L. Mallory,[6] and by M. Sayer and W. R. Hardy[7] seemed to indicate the existence of carrier trapping centers that enhance the efficiency of CaWO$_4$ as a nuclear particle counter. The material used however were of unknown chemical and crystal quality, so it was felt that a systematic materials characterization program of CaWO$_4$ is essential before under-taking further scintillation studies. These then are some of the questions that led to the investigation of defect centers produced by fast neutrons, the examination of the metastable ESR centers produced by gamma radiations, and the identifica-tion of the carrier capture centers responsible for the thermoluminescence of CaWO$_4$.

II. CRYSTAL GROWTH

The bulk of the crystals used in the experiments were grown by R. T. Farrar of the Harry Diamond Laboratories, Washington, D. C. using the Czochralski technique in an apparatus similar to that described by Nassau and Broyer.[8] Optical-grade calcium tungstate, rare-earth oxides of 99.97 % purity, and reagent-grade vanadium or niobium pentoxide were used in an iridium crucible. The melt temperature was sensed by a jacketed platinum-platinum/rhodium thermoco-uple in the melt and was stabilized to about ±2.5°C by the automatic adjustment of the r. f. generator power output. The use of a slightly conical alumina chimney above the crucible reduced markedly the temperature fluctuations on the melt surface and resulted in improved uniformity and optical quality of the crystals. The growth interface was still of the desirable conical shape. Pulling was per-formed in air with typical growth speeds of 0.25 to 0.30 in/hr and turning rates ranging from 60-120 rpm.

At the Bendix Reseach Laboratories,[9] the growth temperature control of about 2-4°C was achieved by measuring the temperature of the crucible surface emis-sivity through a sapphire light pipe connected to a radiometer head. This control technique insured that melt was not contaminated by insertion of a thermocouple in the melt.

III. ESR AND ENDOR

A brief discussion of certain aspects of ESR relevant to the study of radia-tion effect will be given. The usefulness of this technique stems from that the fact that the electron can be thought of as a small magnetic and electric probe.

In a magnetic field, the electron can assume two possible orientations giving the energy level diagram shown in Fig. 1. Here β is the Bohr magneton and g is a measure of the electron effective magnetic moment. If the electron were free $g = g_e = 2.0023$. If this were all, the resonance absorption of an electron in a
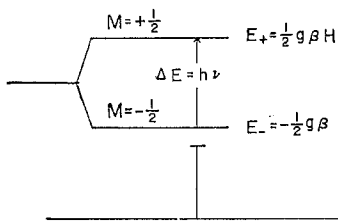
Fig. 1. Electron Zeeman effect. The g-value, a measure of the electron magnetic moment, is sensitive to both crystal direction and environment.
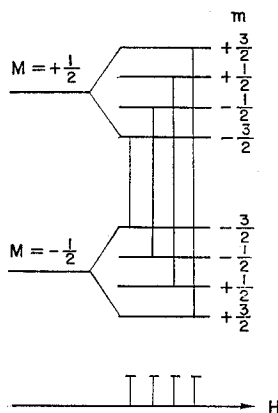

Fig. 2. Hyperfine structure (HFS) and paramagnetic resonance signature. The absorption spectrum consists of the $2I+1$ allowed $(\Delta m=0)$ lines of almost equal intensities and spacings.

magnetic field would have very little interest. Fortunately, the magnitude of the g-value depends critically upon the direction in the crystalline medium and varies from one crystal to another. The g-value is a measure of the internal electric and magnetic fields; it is obtained by measuring the resonance absorption frequency, given by

$$h\upsilon = \Delta E = g\beta H \tag{1}$$

so that

$$g = \frac{h\upsilon}{\beta H} \tag{2}$$

Since the Bohr magneton β and the Planck's constant h are known, the g-values can be obtained from the resonance frequency and the magnetic field.

Furthermore, the hyper-fine structure (HFS) makes it possible to pin-point the nucleus about which the electron is centered. This can be called the paramagnetic resonance signature because it is characteristic of a particular element. The signature is determined by the abundance of the isotopes and their nuclear spins. For example, if a nucleus has spin $I=3/2$, 4 nuclear orientations in a magnetic field are possible, as shown in the accompanying diagram (Fig. 2). Transitions from the lower to the upper electron levels take place, as indicated by the vertical arrows, giving a spectrum of 4 lines of almost equal intensity and equal spacing. If the element consists 100 % of this isotope then the paramagnetic resonance signature is a spectrum of 4 lines as indicated. If the element is a mixture of isotopes, the spectrum is a superposition of such HFS spectra, the intensity being weighted by the abundance. The paramagnetic resonance signature can be computed from

$$\frac{\text{Isotope Abundance}}{2I+1} \tag{3}$$

For example, consider tungsten which consists of the even isotopes 180, 182, 184

and 186, whose combined abundance is 85.77 % and of the odd isotope [183]W, whose spin is 1/2 and abundance 14.24 %. The paramagnetic resonance signature of W then is a triplet with intensities in the ratio 7.12 : 85.77 : 7.12, or about 1 : 12 : 1.

The next problem is to determine the charge on the center. Since the charge on the non-paramagnetic center is known, the charge on the radiation-induced center can be expected to be one less or one more. Thus the electron spin of the metastable center produced by radiation is expected to be 1/2. The electron spin is determined by the number of groups of HFS lines. If the electron spin is S, then its signature is expected to consist of $2S$ groups of $2I+1$ lines. Observations show that almost invariably only one group of HFS lines is present.

There is no general rule by which it is possible to ascertain whether the center is due to capture or loss of an electron. Fortunately, however, for $CaWO_4$, the radicals concerned are tungstate and others formed by substituting for W, such as NbO_4^{3-}, VO_4^{3-}, etc. These radicals are very nearly tetrahedral so that charge assignments can be made with considerable degree of confidence by using the so-called Wolfsberg-Helmholz and Ballhausen-Liehr theory.[10] The theory is concerned with the sequence of electron energy levels in tetrahedral molecules. Their theory, based partly upon calculations and partly upon experimental results, states that the sequence of energy levels is t_1, e, and t_2.

These energy levels are the analogues of the "electron shells" in atomic structure. For example consider V^{5+}. This ion has 18 electrons, with the electrons in the 1 s-, 2 s-, 2 p-, 3 s-, and 3 p-shells. The highest filled shell is 3 p, and the shell above it is 3 d. Consequently the electron configurations for V^{6+}, V^{5+}, and V^{4+} are as follows (Fig. 3).
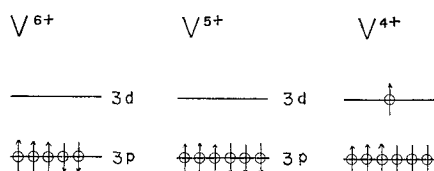

Fig. 3. Electron configuration of V^{6+}, V^{5+}, and V^{4+}. The filled 1 s-, 2 s-, 2 p-, and 3 s- electron shells are not shown. For both V^{5+} and V^{4+}, the 3 p-shell contains the full quota of 6 electrons, but for V^{6+} the 3 p-shell is short of one electron from a full shell. The notation s, p, d, etc. refer to the irreducible representations of the spherical (infinitesimal rotation) group.

This concept of electron shells can be extended to molecules. We might call them molecular electron shells. As an example consider the tungstate radical WO_4^{2-}, which is an example of a 32 electron system.[10] The molecular skeleton consists of the tungsten ion W^{6+}, surrounded by 4 oxygen ions, each having +6 charges. If the 32 electrons are added to this molecular skeleton, then the highest filled shell is considered to be t_1 according to the WH-BL theory, and the next two shells are e and t_2. Hence the expected electron configurations for WO_4^-, WO_4^{2-}, and WO_4^{3-} are as shown below (Fig. 4). And by fairly general arguments, it can be shown that if the unpaired electron is in the e-level, Δg is negative with
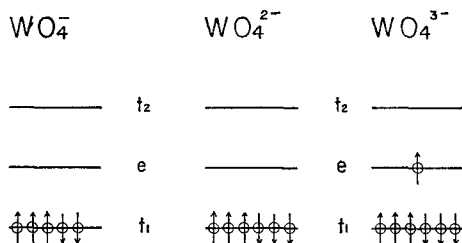
$$WO_4^{-} \qquad WO_4^{2-} \qquad WO_4^{3-}$$

Fig. 4. Molecular electron levels of tetrahedral MO_4 molecules, in which M is a transition metal ion. The relations t_1, e, t_2 are three of the 5 irreducible representations of the tetrahedral (T_d) group.

a large HFS, but for a hole in the t_1-shell, the Δg is positive* and the HFS is small.

Although these are the general "guide lines" for charge assignments, other experimental results need to be considered before the final assignment is made.

The consistency of the WH-BL level sequence with ESR resuts has been shown by D. S. Schonland[11] and others.[12]

An important modification of the ESR experiment is the so-called ENDOR (Electron Nuclear Double Resonance) technique. In this method a second frequency in the RF range is used to probe the spacing of hyperfine structure (HFS) levels. To see how the experiment works, consider the following diagram (Fig. 5).
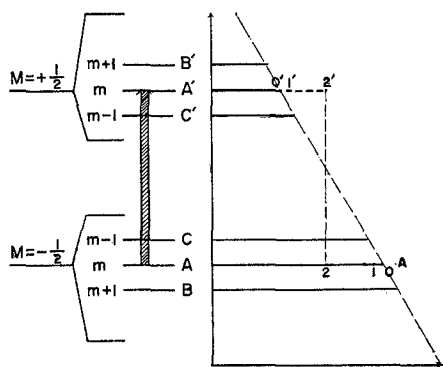

Fig. 5. Energy levels and spin populations. As the power level of the pump signal, for example AA', is increased, the populations of A and A' approach equality and the deviation from the thermal equilibrium distribution increases.

On the left hand side three HFS levels for each of the electron Zeeman levels are shown. In labeling these levels, it is assumed that the HFS coupling constant A is positive. The plot on the right-hand side shows the population, $i.\,e.$, the number of spins in each state. At thermal equilibrium (when no signal is applied) the population distribution follows the Maxwell relation

* $\Delta g = g - g_e = g - 2.0023$

$$\exp(-E/kT) \qquad\qquad (4)$$

given by the dotted exponential curve. Suppose now an ESR signal is turned on, as indicated by the thick arrow. The effect of such a signal is to "pump" spins from the lower state A into the higher state A'. There will then result a deviation from the Maxwellian distribution. If the power level of the ESR signal is low, as is the case for the usual ESR experiments, the deviation from the Maxwellian distribution is small, possibly represented by points 1 and 1'. If, however, the power level is raised, the pumping rate from A into A' will become greater, and the population of the upper state will continue to increase at the expense of the lower one. Eventually, at extremely high power level, the population of A' can become almost equal to that of A. This situation is depicted by the points 2 and 2'.

When this occurs, we note that the population of A is considerably smaller than those of B and C, whereas the population of A' is much greater than those of B' and C'. Suppose then an RF signal is applied just matching the separation of, say, A'B'. This will drain the spins from state A' into B', resulting once more in a population difference between A and A', therefore giving an increase in absorption of power at ESR frequency.

Therefore to carry out the experiment, the changes in the microwave power absorption is noted upon sweeping the RF through a range of frequencies. The range of the RF generator can be readily determined from the separation of the HFS levels. The spacings are of the order A/2. Consequently
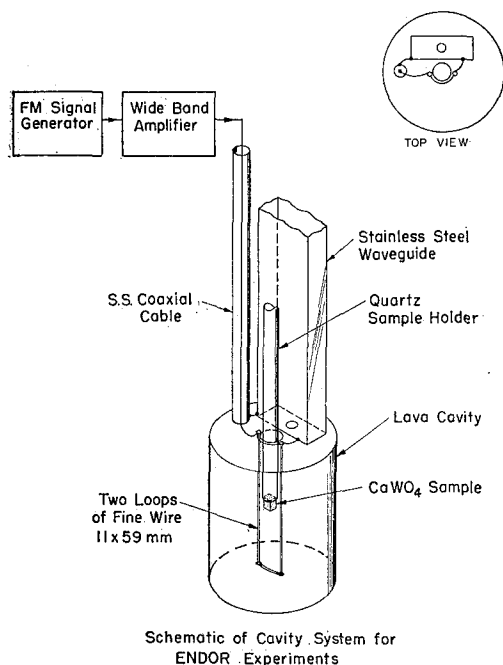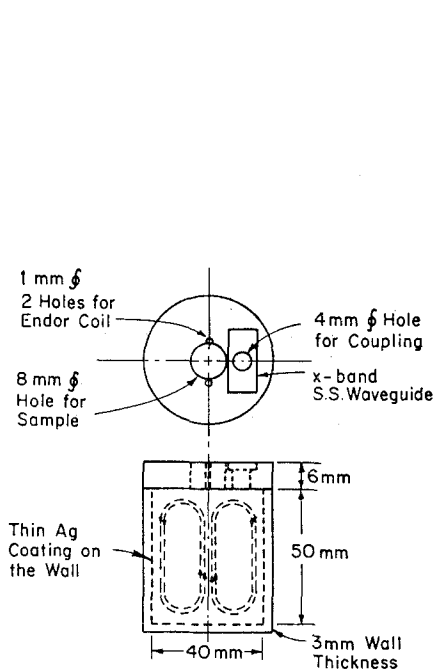
Fig. 6. Cavity system for ENDOR experiments.

Fig. 7. Details of lava cavity and magnetic field configuration for TE_{011} mode.

$$\bar{\nu} = \frac{g\beta A}{2ch} \tag{5}$$

and therefore

$$\nu = \frac{c}{\lambda} = \frac{g\beta A}{2h} \tag{6}$$

Since A is about 30 gauss, the above expression gives about 46 MHz.

Some of the details of the experiment to carry out the ENDOR measurements are shown in Fig. 6. The cylindrical microwave cavity is designed for the TE_{011} mode, for which the magnetic field configuration is as shown in Fig. 7. The ENDOR RF signal was obtained from an FM-AM Standard Signal Generator of Type M 527 made by Radiometer, Denmark. This is followed by two or three Hewlet-Packard hp-460 AR wide band amplifiers connected in cascade. The output is further amplified by two wide band power amplifiers IFI 500 (Instruments for Industry). A typical ENDOR spectrum taken with this experimental arrangement is shown in Fig. 8.

But how are the four experimental frequencies (Fig. 8) to be related to the transitions A↔B, A↔C, A'↔B', and A'↔C' of Fig. 5? To see how this is to be done consider the eigenvalue

$$E(M, m) = g\beta HM + AMm + 1/2 Q_{33}[3m^2 - I(I+1)] - g_n\beta_N Hm \tag{7}$$

of the Hamiltonian

$$H = g\beta H \cdot S + AI \cdot S + I \cdot Q \cdot I - g_n\beta_N H \cdot I \tag{7'}$$

We shall limit our discussion to the case for $S = 1/2$, so that in (7), $M = \pm 1/2$. The ENDOR frequency assignment is dependent upon the sign of A. The energy level diagrams for the two cases of positive and negative A are shown below in Fig. 9. For $A > 0$, we obtain from (7)

$$\left.\begin{aligned}
\nu_1 &= \frac{1}{2}A + \frac{3}{2}Q_{33}(2m+1) - g_n\beta_N H \\
\nu_2 &= \frac{1}{2}A + \frac{3}{2}Q_{33}(2m-1) - g_n\beta_N H \\
\nu_3 &= \frac{1}{2}A - \frac{3}{2}Q_{33}(2m-1) + g_n\beta_N H \\
\nu_4 &= \frac{1}{2}A - \frac{3}{2}Q_{33}(2m+1) + g_n\beta_N H
\end{aligned}\right\} \tag{8}$$

whereas for $A < 0$, we obtain

$$\left.\begin{aligned}
\nu_1 &= \frac{1}{2}|A| - \frac{3}{2}Q_{33}(2m-1) + g_n\beta_N H \\
\nu_2 &= \frac{1}{2}|A| - \frac{3}{2}Q_{33}(2m+1) + g_n\beta_N H \\
\nu_3 &= \frac{1}{2}|A| + \frac{3}{2}Q_{33}(2m+1) - g_n\beta_N H \\
\nu_4 &= \frac{1}{2}|A| + \frac{3}{2}Q_{33}(2m-1) - g_n\beta_N H
\end{aligned}\right\} \tag{8'}$$

If then these ENDOR frequencies are plotted as functions of we obtain for $Q_{33} < 0$ and for $Q_{33} < 0$ the plots shown in Figs. 10 a and 10 b respectively.
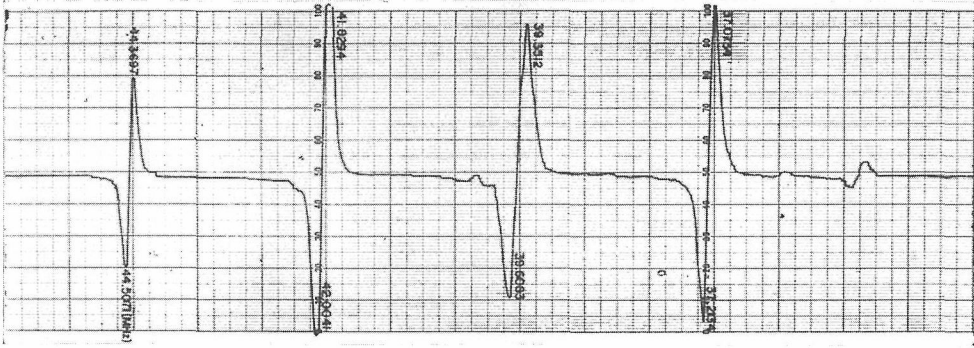
Fig. 8. ENDOR spectrum for magnetic field along c-axis. For this, the saturating micro-wave power was applied to the $m=1/2$ line.
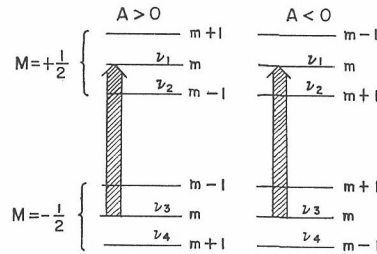

Fig. 9. Hyperfine structure levels contributing to ENDOR spectrum when the ESR line m is saturated. The vertical thick arrow indicates that the saturating microwave power is applied between the levels m of $M=\pm 1/2$.
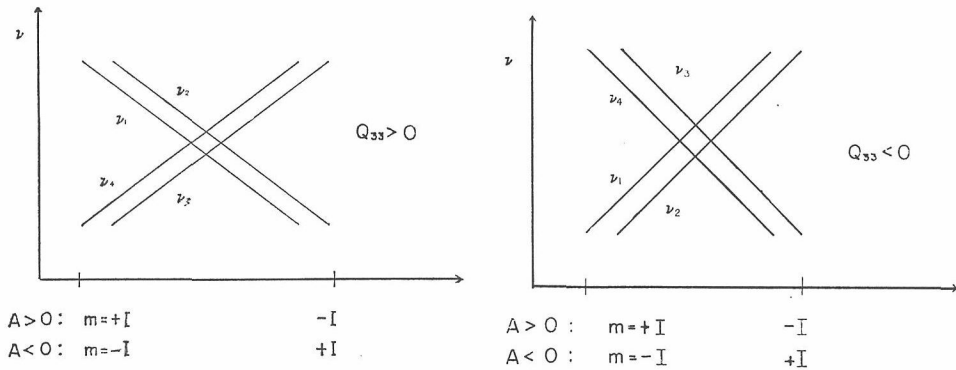
Fig. 10 a. ENDOR frequency plot for $Q_{33}>0$. Fig. 10 b. ENDOR frequency plot for $Q_{33}<0$.

The use of these plots for the interpretation of Nb^{4+} ENDOR measurements will be discussed presently.

IV. CRYSTAL STRUCTURE

To interpret the ESR spectrum of Nb^{++}, the relative positions of coupled impurity and/or vacancy is important. For this the crystal structure is needed. Consequently, we shall discuss the structure of CaWO$_4$.

(17)

The structure of the $CaWO_4$ crystal is quite complex, as shown in Fig. 11. The space group is No. 88 in the International Tables for x-Ray Crystallography, designated as $I\,4_1/a$, or C^6_{4h} in Schoenflies notation. Recently, refined x-ray diffraction measurements have been reported by A. Zalkin and D. H. Templeton[13] and the neutron diffraction measurements by M. I. Kay, B. C. Fraser, and I. Almodovar.[14] These measurements provided precise information of oxygen positions. The cell parameters of $CaWO_4$ are

$$a_e = b_o = 5.243\ A$$

$$c_o = 11.376\ A$$

with the atoms located at

$$(0,\ 0,\ 0\,;\,1/2,\ 1/2,\ 1/2)$$

$$4\,Ca\ at\ (0,\ 01/2)\,;\,0,\ 1/2,\ 3/4$$

$$4\,W\ at\ 0\ 0\ 0\,;\,0\ 1/2\ 1/2$$

$$16\,0\ at\ (x,\ y),\ z\,;\,(y,\ x)\ y,\ z$$

$$(x,\ 1/2\text{-}y),\ 1/4\text{-}z$$

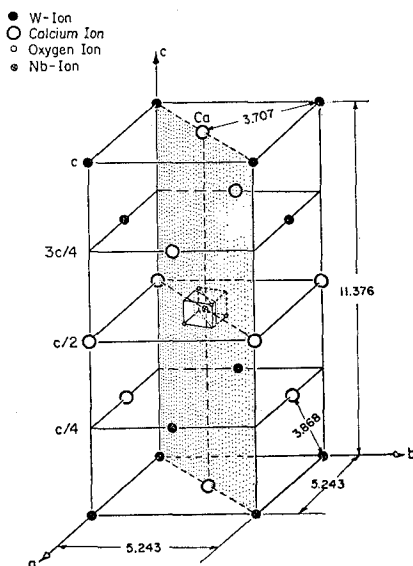$$(y,\ 1/2\text{-}y),\ 1/4\text{-}z$$

Fig. 11. Unit cell of $CaWO_4$.

The oxygen coordinates using a W atom as the origin are as follows:

$$x = (0.2415 \pm 0.0014)\,a_0,$$

$$y = (0.1504 \pm 0.0013)\,a_0,$$

$$z = (0.0816 \pm 0.0006)\,c_0.$$

The structure of calcium tungstate crystal may be viewed as composed of tungstate WO_4 radicals bonded ionically to calcium Ca^{++} cations. The metal

sites are found on planes separated by a distance of 2.844A from each other and perpendicular to the c-axis. The local site symmetry of both calcium and tungsten is S_4. Each tungsten is bonded to four nearest oxygen to form a slightly squashed tetrahedron with the W-O bond distance of 1.783A. The O-W-O are 113°27′ (twice) and 107°56′ (four times). The WO_4^{--} bisphenoid (tetrahedron distorted along one of the two-fold axes) and its projection on the (a, b) plane are shown in Fig. 12.
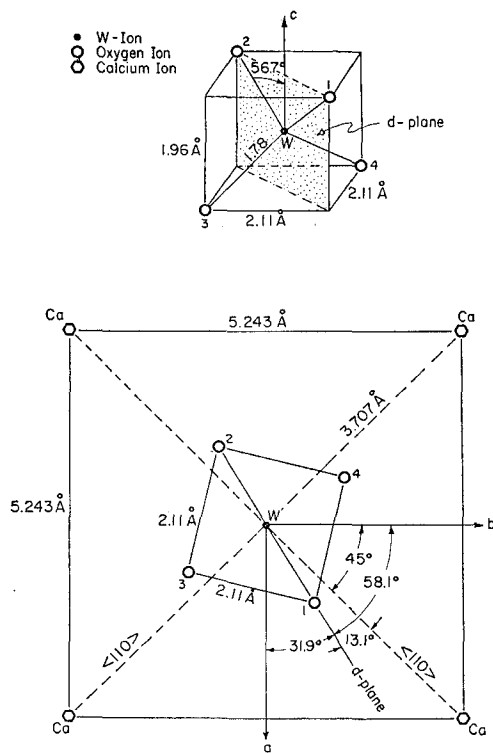

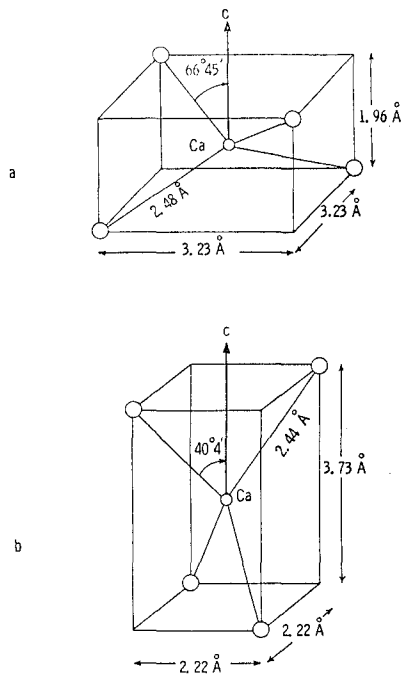Fig. 12. Structure of tungstate radical.

Fig. 13. Oxygens surrounding calcium.

The nearest neighbors of the calcium atoms are the eight oxygens at the vertices of two different bisphenoids as shown in Fig. 13. The Ca-O distances are 2.44A and 2.48A respectively.

In the designation $I4_1/a$ introduced earlier, the symbol I stands for body-centered structures, 4_1 indicates a four-fold screw-axis, and a denotes a glide along the a-axis, i.e., a translation of a/2 followed by reflections in planes normal to the c-axis. The glide planes are located at $z=1/8$, 3/8, 5/8, and 7/8. The Schoenflies notation C^6_{4h} denotes that the space group is isomorphic with the point group C_{4h}, in which the 4-fold axis is replaced by a 4-fold screw axis.

The crystal structure can be thought of as layers of planes with the stacking sequence ABCDA······, in which each plane consists of an interlocking square lattice of Ca and WO_4^{--} radicals. The Ca and W atoms lie in tha same plane. The atoms in the other planes (BCD) are generated by the a-glides. The nearest Ca_I sites are located 3.71A at 45° from the a-axis in the ab plane. The Ca_{II}-sites

on the other hand are at 3.87A, in the ac- or bc-plane, making 42°40′ with the c-axis.

V. Nb IN CaWO₄

As indicated earlier, this study was undertaken because the co-doping of CaWO$_4$ with both Nd and Nb results in a substantial reduction of the laser threshold.   The ESR of Nb^{4+} in CaWO$_4$ was first reported by K. C. Chu, C. Kikuchi, and W. Viehmann[19] and most recently Dr. D. L. Tseng,[29] now at Tsing Hua University, Taiwan, has made careful systematic ESR and ENDOR measurements.

The portion of the periodic table of concern to the present study is given by

Group V	Group VI	Electron
V	Cr	3d
Nb	Mo	4d
Ta	W	5d

The paramagnetic properties arise primarily from the electron being in the 3d-, 4d-, or 5d- orbit for the elements in different rows.   The ESR properties for the ions in a single column, such as V, Nb, and Ta are expected to be similar, and indeed found to be so.   The only conspicuous difference arise from the nuclear electric quadrupole moments which increase by an order of magnitude going from V to Nb and then to Ta.   Thus ESR spectra are superficially quite different.

The samples were prepared by first accurately mounting the cut sample on a vycor quartz rod and then irradiating in the Phoenix Memorial Laboratory 10 Kc Co-60 source for 1 to 2 hours.   The dose rate was about 200 Krads per hour.   The sample irradiated at 77°K is transferred into the pre-cooled cavity as
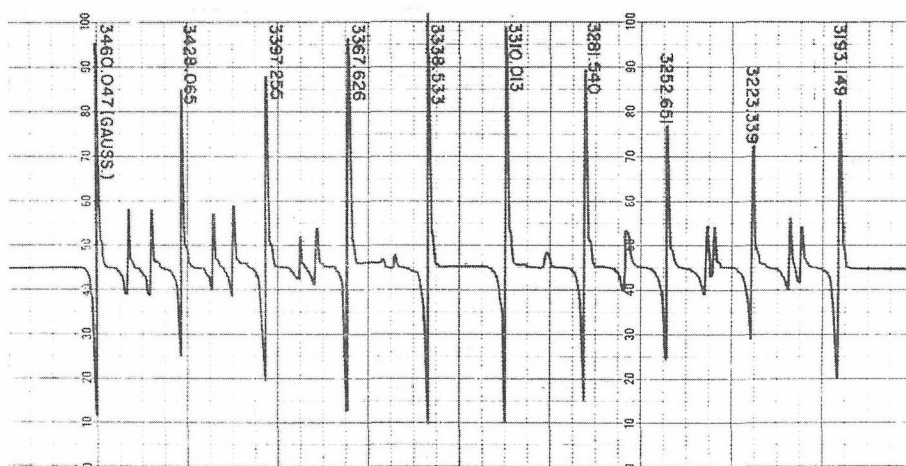

Fig. 14.   ESR spectrum of Nb^{4+} in gamma irradiated CaWO$_4$. The sample was irradiated and measured at 77°K.   The magnetic field is along the c-axis.

quickly as possible.

In Fig. 14 a typical ESR spectrum for Nb^{4+} is given. The spectrum shows several unusual features. We note that the 10 HFS lines, for the 100% ^{93}Nb whose nucler spin is 9/2, are almost equally spaced, but the intensity distribution is rather unusual. The central HFS components are the strongest, the intensities taper downward going outward from the center and is the least for the lines $m = \pm 7/2$. There are also the conspicuous doublets, whose intensities drop going inwards to the center of the spectrum, where it is zero. Furthermore upon careful measurements, it is found that there is measurable deviations from the equal spacing of the HFS lines; the lines are actually closest at the center, and fatherest apart in the wings.

These features of the ESR spectrum can be readily accounted for by assuming a strong nuclear electric quadrupole interaction. To prove these points, consider the spin-Hamiltonian

$$H = g\beta H \cdot S + AI \cdot S + I \cdot Q \cdot I - g_n\beta_N H \cdot I,$$

In this Hamiltonian, the assumption is that the electron g-tensor, the hyperfine structure A-tensor, and the nuclear g-tensors are isotropic and hence scalars. Measurements show that there are small anisotropies. However these anisotropies are small in comparison to that of the quadrupole term, so that the essential features of the ESR spectrum can be obtained from the above Hamiltonian.

If M and m denote the electron and the nuclear magnetic quantum numbers, respectively, it is easy to show from perturbation calculation that the eigenvalues are given by

$$E(M, m) = g\beta H M + AMm + <m|I \cdot Q \cdot I|m>$$
$$- g_n\beta_N H m + \sum \frac{|<m'|I \cdot Q \cdot I|m>|^2}{AMm - AMm'}, \qquad (9)$$

and the associated wave functions to the first order by

$$\psi_{Mm} = \varphi_M \left[\varkappa_m + \sum_{m'} \frac{<m'|I \cdot Q \cdot I|m>}{AM(m-m')} \varkappa_{m'} \right], \qquad (10)$$

in which φ_M and $\varkappa_m$ are the eigen-functions of the electron and nuclear spin operators respectively, namely

$$S^2\varphi_M = \frac{3}{4}\varphi_M \qquad I^2\varkappa_m = I(I+1)\varkappa_m, \left.\begin{array}{c} \\ \\ \\ \end{array}\right\}$$
$$S_z\varphi_M = M\varphi_M \qquad I_z\varkappa_m = m\varkappa_m. \qquad (11)$$

In ESR measurements, the transitions are such that $\Delta M = \pm 1$. The intensities for such transitions are given by

$$|<M+1, m|S_+|mM>|^2. \qquad (12)$$

We find then that the relative intensities of the "allowed" transitions $\Delta m = 0$ are given by

$$\left| 1 - \frac{4}{A^2} \sum \left| \frac{<m'|I \cdot Q \cdot I|m>}{m-m'} \right|^2 \right|^2 \sim 1 - \frac{8}{A^2} \sum_{m'=m-2}^{m+2} \left| \frac{<m'|I \cdot Q \cdot I|m>}{m-m'} \right|^2. \qquad (13)$$

For the first forbidden transitions $(\Delta m = \pm 1)$, we have

$$\frac{16}{A^2}|<m\pm1|I\cdot Q\cdot I|m>|^2,\tag{14}$$

and for the second forbidden $\varDelta m=\pm2$ lines

$$\frac{4}{A'}|<m\pm2|I\cdot Q\cdot I|m>|^2.\tag{15}$$

The matrix elements can be evaluated by noting that

$$
\begin{aligned}
I\cdot Q\cdot I \\
&=\frac{1}{2}Q_{33}[3I_z^2-I(I+1)] \\
&=\frac{1}{2}(Q_{13}-iQ_{23})[I_+I_z+I_zI_+] \\
&=\frac{1}{2}(Q_{13}+iQ_{23})[I_-I_z+I_zI_-] \\
&=\frac{1}{4}(Q_{11}-Q_{22}-2iQ_{12})I_+^2+\frac{1}{4}(Q_{11}-Q_{22}+2iQ_{12})I_-^2.
\end{aligned}\tag{16}
$$

For the relative intensities of the allowed lines, we obtain

$$1-\frac{8}{A^2}\frac{1}{4}(Q_{13}^2+Q_{23}^2)$$
$$\times[(2m+1)^2\{I(I+1)-m(m+1)\}+(2m-1)^2\{I(I+1)-m(m-1)\}],\tag{17}$$

upon neglecting the effects of the second forbidden transitions. We find then for the reduction in the relative intensities is given by the ratio

$$12:24:19:9:2:2:9:19:24:12.\tag{18}$$

Thus the lines $m=\pm7/2$ suffers the most reduction in intensity and the lines $m=\pm1/2$ undergo the least reduction. These are the weakest and the strongest lines respectively.

Similarly, the relative intensities of the first forbidden lines are given by

$$(2m\pm1)^2[I(I+1)-m(m\pm1)]\frac{4}{A^2}(Q_{13}^2+Q_{23}^2),\tag{19}$$

which gives the ratio

$$24:24:14:4:0:4:14:24:24,\tag{20}$$

and for the second forbidden transitions, we have

$$\frac{1}{4A^2}[(Q_{11}-Q_{22})^2+4Q_{12}^2][I(I+1)-m(m\pm1)][I(I+1)-(m\pm1)(m\pm2)],\tag{21}$$

giving the ratio

$$6:14:21:25:25:21:14:6.\tag{22}$$

Comparing the coefficients for the first and the second forbidden lines, we see that the second forbidden lines are an order of magnitude weaker than the first forbidden lines.

For the eigenvalues we can easily show that

$$
\begin{aligned}
E(M,m)=g\beta HM+(A+A')m+BMm^3 \\
+\frac{1}{2}Q_{33}gm^2-I(I+1)]-g_n\beta_NHm,
\end{aligned}\tag{23}
$$

in which

$$A' \equiv \frac{1}{A}[Q_{13}^2 + Q_{23}^2)\{8I(I+1)-2\} + \{(Q_{11}-Q_{22})^2 + 4Q_{12}^2\}\{8I(I+1)-4\}], \quad (24)$$

and

$$B \equiv \frac{1}{A}[16(Q_{13}^2+Q_{23}^2) - \{(Q_{11}-Q_{22})^2 + 4Q_{12}^2\}]. \quad (25)$$

For the allowed transitions, $\Delta m = 0$, we find that

$$E\left(\frac{1}{2}, m\right) - E\left(-\frac{1}{2}, m\right) = g\beta HM + (A+A')m + Bm^2, \quad (26)$$

so that the HFS separations are expected to show the quadratic dependence on m. For the first forbidden transitions, $\Delta m = \pm 1$ we obtain

$$E\left(\frac{1}{2}, m+1\right) - E\left(-\frac{1}{2}, m\right) = g\beta H + \frac{1}{2}(A+A')(2m+1)$$
$$+ \frac{1}{2}B[(m+1)^3 + m^3] + \frac{3}{2}Q_{33}(2m+1) - g_n\beta_N H, \quad (27)$$

and

$$E\left(\frac{1}{2}, m\right) - E\left(-\frac{1}{2}, m+1\right) = g\beta H + \frac{1}{2}(A+A')(2m+1)$$
$$+ \frac{1}{2}B[(m+1)^3 + m^3] - \frac{3}{2}Q_{33}(2m+1) + g_n\beta_N H, \quad (28)$$

so that the first forbidden doublets are separated by

$$3Q_{33}(2m+1) - 2g_n\beta_N H. \quad (29)$$

We can obtain the sign of Q_{33} by examining the m-dependence of the doublet separation. Starting at the low-field end, we notice that the separation at first decreases, and then increases, indicating that the positions of the two first forbidden doublets become reversed. This means that both g_n and Q_{33} have the same sign, and since g_n is known to be positive, we deduce that Q_{33} is also positive.

For the second forbidden transitions we have

$$E\left(\frac{1}{2}, m+2\right) - E\left(-\frac{1}{2}, m\right) = g\beta H + \frac{1}{2}(A+A')(2m+2)$$
$$+ \frac{1}{2}B[(m+2)^3 + m^3] + \frac{3}{2}Q_{33}(4m+4) - 2g_n\beta_N H, \quad (30)$$

and

$$E\left(\frac{1}{2}, m\right) - E\left(-\frac{1}{2}, m+2\right) = g\beta H + \frac{1}{2}(A+A')(2m+2)$$
$$+ \frac{1}{2}B[(m+2)^3 + m^3] - \frac{3}{2}Q_{33}(4m+4) + 2g_n\beta_N H. \quad (30')$$

Thus we see that the two lines flank the

$$\frac{1}{2}(m+m+2), \quad (31)$$

allowed HFS lines and the doublet separations are

$$6Q_{33}(2m+2)-4g_n\beta_N\mathrm{H}. \tag{32}$$

These have not been looked for and hence not analyzed. The reason is that the intensities are weak, possibly comparable to the superhyperfine structure on the HFS lines due to ^{183}W. The evidence for the superhyperfine structure comes from the structure of the $m=\pm9/2$ lines; the second forbidden transitions are not expected to contribute to the structure of these lines.

The expression for the intensities of the first forbidden lines is useful in determining the directions of the quadrupole principal axes. The quantities Q_{13} and Q_{23} are the off-diagonal components of the quadrupole interaction term in a coordinate system in which the 3-axis is along the magnetic field. Consequently, if the magnetic is along one of the quadrupole principal axis, both Q_{13} and Q_{23} will be zero, so that the first forbidden line intensities are zero. Such directions give the quadrupole axes.

Since one of the aims of the program was to obtain information about charge compensation, it was our hope to link the anisotropy in certain ESR measurements, such as the quadrupole effect, to the charge compensating pair axis. If this can be done, then according to Fig. 11, we note that a quadrupole axis can be expected to be along the [110] direction if the pair occupy nearest Ca- and and W-sites, in the ac- or bc- plane making $42°40'$ with the c-axis if the pair occupy second nearest sites, etc. In Fig. 15 we show the ESR spectrum taken

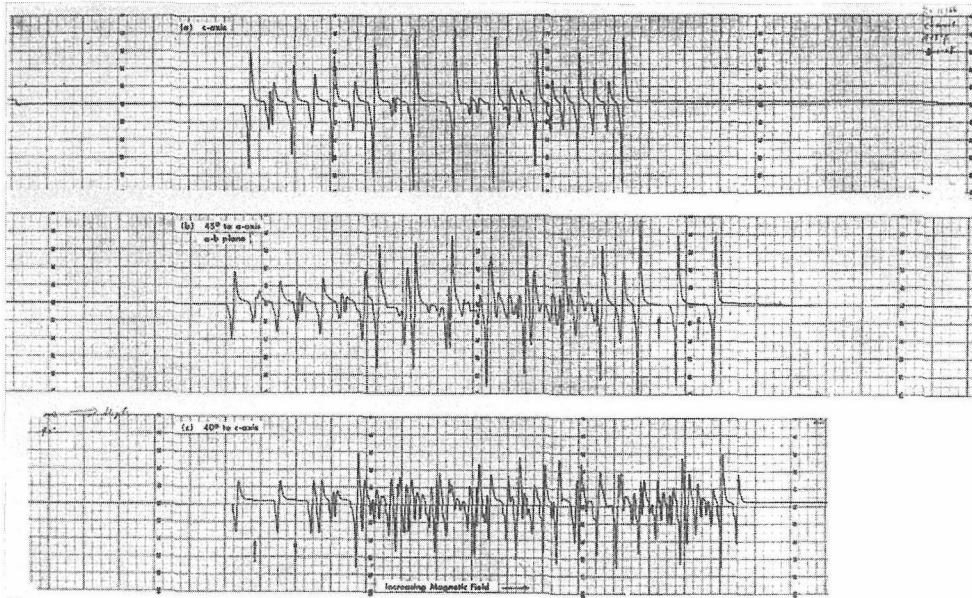Fig. 15. Forbidden line spectra along quadrupole principal axes. The vertical arrows in traces (b) and (c) indicate the missing first forbidden doublets.

along the [110] direction. The vertical arrows show the positions of the missing lines. Another axis, of course, lies in a plane perpendicular to this direction and therefore in the [110]-planes. As shown the doublets again are absent for $\theta=33°$ in the (110) planes.

The precision values of the quadrupole interaction are obtained by ENDOR measurements. From the expression for the eigenvalues given earlier, we find for the separation between adjacent nuclear Zeeman levels

$$E(M, m+1) - E(M, m) = (A+A')M + [(m+1)^3 - m^3]MB$$
$$- g_n\beta_N H + \frac{3}{2}Q_{33}[(m+)^2 - m^2], \tag{33}$$

$$E(M, m) - E(M, m-1) = (A+A')M + BM[m^3 - (m-1)^3]$$
$$- g_n\beta_N H + \frac{3}{2}Q_{33}[m^2 - (m-1)^2]. \tag{33'}$$

For sake of definiteness, assume that A is positive. Then for $M=+1/2$ the nuclear Zeeman levels are in the order, $m-1$, m, $m+1$ the last being the highest, but for $M=-1/2$, the order is $m+1$, m, $m-1$, the $m+1$ state being the lowest. The measured frequencies then are given by

$$\left.\begin{aligned}
h\nu_1 &= \frac{1}{2}(A+A') + \frac{1}{2}B[(m+1)^3 - m^3] - g_n\beta_N H + \frac{3}{2}Q_{33}(2m+1), \\[6pt]
h\nu_2 &= \frac{1}{2}(A+A') + \frac{1}{2}B[m^3 - (m-1)^3] - g_n\beta_N H + \frac{3}{2}Q_{33}(2m-1), \\[6pt]
h\nu_3 &= \frac{1}{2}(A+A') + \frac{1}{2}B[(m+1)^3 - m^3] + g_n\beta_N H - \frac{3}{2}Q_{33}(2m+1), \\[6pt]
h\nu_4 &= \frac{1}{2}(A+A') + \frac{1}{2}B[m^3 - (m-1)^3] + g_n\beta_N H - \frac{3}{2}Q_{33}(2m-1),
\end{aligned}\right\} \tag{34}$$

in which we have defined

$$\left.\begin{aligned}
\nu_1 &\equiv \nu\left(M=+\frac{1}{2}, \ m\to m+1\right), \\[6pt]
\nu_2 &\equiv \nu\left(M=+\frac{1}{2}, \ m-1\to m\right), \\[6pt]
\nu_3 &\equiv \nu\left(M=-\frac{1}{2}, \ m\to m-1\right), \\[6pt]
\nu_4 &\equiv \nu\left(M=-\frac{1}{2}, \ m+1\to m\right),
\end{aligned}\right\} \tag{35}$$

Then

$$\left.\begin{aligned}
h(\nu_1+\nu_2+\nu_3+\nu_4) &= 2(A+A') + B(6m^2+2), \\[4pt]
h(\nu_1-\nu_2-\nu_3-\nu_4) &= 6Q_{33}, \\[4pt]
h(\nu_1+\nu_2-\nu_3-\nu_4) &= -4g_n\beta_N H + 12Q_{33}, \\[4pt]
h(\nu_1-\nu_2+\nu_3-\nu_4) &= 6mB.
\end{aligned}\right\} \tag{36}$$

By applying the saturating microwave to different HFS lines, plots, such as shown in Figs. 16, 17 and 18 are obtained. The magnetic field increases from left to right, i.e. the line labeled 9/2 is the low-field HFS line. The plots consist of four curves, which can be concave upward, downward, or even straight lines. We note however the curvatures for a given plot are the same, i.e., the plots are either all concave upward or all concave downward. These are to be expected, as can be seen from Eq. (34). The curvature of the plots are determin-
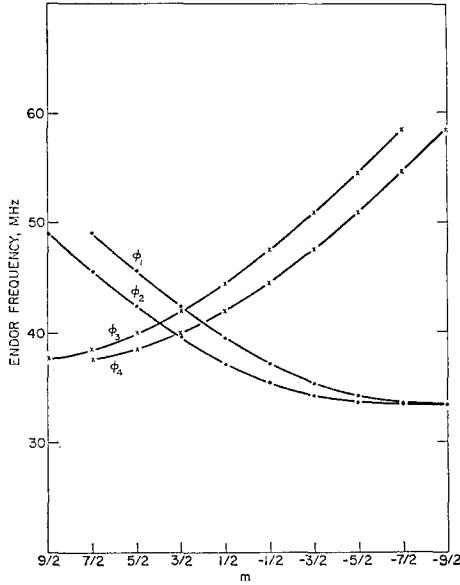
Fig. 16. ENDOR frequency plot for magnetic field along c-axis. Note that the plots are concave upward.
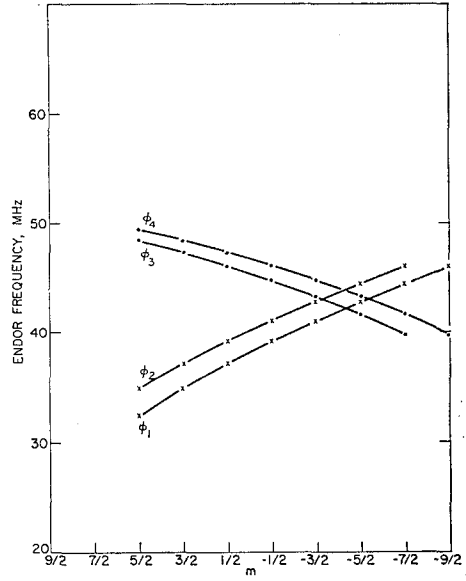
Fig. 17. ENDOR frequency plot for magnetic field along x_θ-axis ($\theta=57°$, $\varphi=225°$). Note that the plots are concave downward.

Fig. 18. ENDOR frequency plot for magnetic field along y_θ-axis ($\theta=90°$, $\varphi=-45°$).

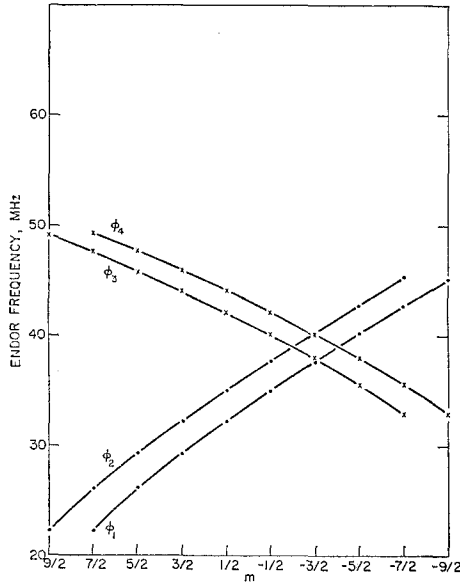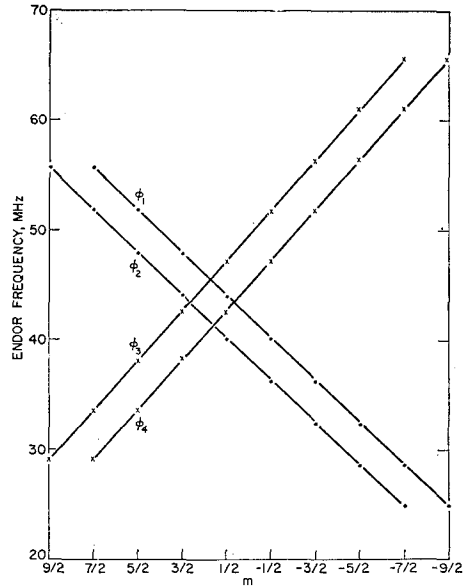Fig. 19. ENDOR frequency plot for magnetic field along z_θ-axis ($\theta=33°$, $\varphi=45°$). Note that the plots are effectively straight lines.

ed by the coefficient B. Particularly when the magnetic field is along a principal axis, B reduces to

$$B=-\frac{1}{A}(Q_{11}-Q_{22})^2,\qquad(37)$$

and the curvatures are given by

$$A > 0 \qquad +B$$
$$A < 0 \qquad -B$$

so that for both cases the ENDOR frequency plots are expected to be concave downward. Furthermore, we need to note that 1 and 2 in the above expressions refer to the two axes perpendicular to the magnetic field. Consequently, the curvature is the least when the magnetic field is along the major quadrupole principal axis. This point is illustrated by Fig. 19, in which the ENDOR frequency plots are almost straight lines.

Such measurements lead to the following results for the quadrupole and nuclear gyromagnetic ratio tensors :

	θ	φ	Q (MHz)	g_n
z	33°	45°	1.392	1.3657
x	57°	225°	−0.561	1.3446
y	90°	−45°	−0.835	1.3568

Analysis of the ESR spectra lead to the following spin-Hamiltonian parameters :

g-Tensor

	θ	φ	g
z	62°	28°	2.0534
x	28°	208°	2.0133
y	90°	−62°	2.0077

A-Tensor

	θ	φ	A (MHz)
z	62.5°	45°	88.388
x	27.5°	225°	80.979
y	90°	−45°	75.159

We note that the g-values all exceed that of the free electron, namely, 2.0023. This suggests that the center which we are concerned is a hole, namely the radical NbO_4^{2-}. As we shall see later the trap depth for the hole is about 0.72 ev.

VI. ELECTRON TRAPPING CENTERS

As indicated earlier, irradiation of a $CaWO_4$ single crystals results in the release of electron from certain centers and the subsequent trapping of the electrons at other centers. We shall here consider the evidence for electron trapping centers.

The theoretical basis for this assignment, aside from consistency arguments

to be used later, is provided by Wolfsberg-Helmholz-Ballhausen-Liehr theory which suggests that the lowest unfilled level for an MO_4 tetrahedral molecules is e, followed by t_2. That this level scheme is consistent with ESR measurements was first shown by Schonland,[11] and later further supporting evidence was given Banks, Greenblatt, and McGarvey,[12] who investigated that spectrum of CrO_4^{3-} in chlorospodiosite (Ca_2PO_4Cl). The same arguments can be extended to Cr, Mo, and certain W paramagnetic centers in $CaWO_4$.

It is easy to show that the pair of functions d_{z^2} and $d_{x^2-y^2}$ transform like the irreducible representation e of T_d and that d_{xy}, d_{yz} and d_{zx} transform like t_2. Here the d's represent quantities that transform like the polynomials

$$d_{z^2} \propto \frac{1}{2}(3z^2 - r^2),$$

$$d_{x^2-y^2} \propto \frac{\sqrt{3}}{2}(x^2 - y^2),$$

$$d_{xy} \propto \sqrt{3}\, xy,$$

$$d_{yz} \propto \sqrt{3}\, yz,$$

$$d_{zx} \propto \sqrt{3}\, zx.$$

Then according to the WH-BL theory, the wave functions of the lower state are given by d_{z^2} and $d_{x^2-y^2}$ and the higher t_2-level by d_{xy}, d_{yz}, d_{zx}. If the tetrahedron is distorted by compressing along the z-axis, there will be further splittings of the two states, given by Fig. 20.
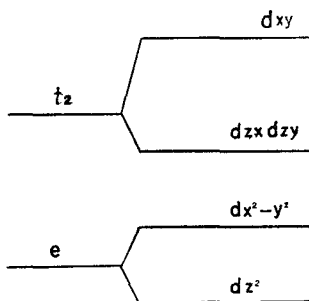
Fig. 20. Effect of bisphenoidal distortion upon tetrahedral energy levels. Upon reducing the symmetry, the lower e-level splits into two singlets and the upper triplet (t_2) splits into a singlet and a doublet.

That d_{z^2} is the lowest state is obtained by analysis of experimental results. If d_{z^2} is the lower of the two, it can be shown that

$$g_{//} = 2.0023,$$

$$g_{\perp} = 2.0023 - \frac{6}{E(zx, zy) - E(z^2)},$$

$$A_{//} = -K + \frac{4}{7}P - \frac{1}{7}(g_{//} - g_e)P,$$

$$A_{\perp} = -K - \frac{2}{7}P - \frac{15}{14}(g_{\perp} - g_e)P,$$

whereas if $d_{x^2-y^2}$ is lowest,

$$g_{//} = g_e - \frac{8}{E(xy) - E(x^2-y^2)},$$

$$g_\perp = g_e - \frac{2}{E(zx, zy) - E(x^2-y^2)},$$

$$A_{//} = -K - \frac{4}{7}P + (g_{//} - g_e)P + \frac{3}{7}(g_\perp - g_e)P,$$

$$A_\perp = -K + \frac{2}{7}P + \frac{11}{14}(g_\perp - g_e)P,$$

in which

$$P = 2.0023 g_n \beta_N \langle r^{-3} \rangle$$

and K is the contact term. From these results, it is seen that

$$g_{//} > g_\perp, \quad A_{//} < A_\perp \quad \text{for } d_{z^2} \text{ lowest,}$$

$$g_{//} < g_\perp, \quad A_{//} > A_\perp \quad \text{for } d_{x^2-y^2} \text{ lowest.}$$

The experimental results are as follows.

	$g_{//}$	$g_\perp$	$A_{//}$ (10^{-4}cm^{-1})	$A_\perp$ (10^{-4}cm^{-1})	Ref.
^{53}Cr	1.988	1.943	4	23	(15)
^{45}Mo	1.987	1.887	8.39	41.18	(16)
^{183}W	1.850	1.587	19.05	53	(vacuum Reduction)

In all of these cases $g_{//} > g_\perp$, $A_{//} < A_\perp$ and therefore supports the assignment that d_{z^2} is lowest.

The above assignments lead to CrO_4^{3-} and MoO_4^{3-}, but considerable care is needed in assigning the W-centers, because there are several, some with $\Delta g < 0$ and others with $\Delta g > 0$. The tentative suggestion here is that the W-centers produced by vacuum reduction, reported by Azarbayejani,[9] the β-center produced by fast neutron irradiation, reported by Chu and Kikuchi,[21] and the so-called high-field center reported by Zeldes and Livingston[18] are WO_4^{3-} coupled with impurities or defects.

Very careful measurements by Azarbayejani[9] indicate that the g-tensor z-axis is tilted slightly away from the c-axis. The results are as follows:

CaWO$_4$: Y (T$\sim$40°K)

	g_{xx}	g_{yy}	g_{zz}
	1.6048	1.5726	1.8491
θ	91.2°	91.4°	1.9°
φ	27°	117°	89.6°

In addition he reports

CaWO$_4$: La (T∼78°K)

	g_{xx}	g_{yy}	g_{zz}
	1.66303	1.53096	1.79419
θ	97°	90°	6.9°
φ	25°	1142°	83.7°

These conters are produced by heating the sample for one to two hours at a temperature of about 900°C under about 10^{-5} torr pressure. The trivalent dopants Y and La were used to stabilize the paramagnetic W-centers. The fact that Y^{3+} and La^{3+}, occupying the Ca^{2+}-site, stabilizes the paramagnetic W-centers provides further evidence for the assignment $WO_4{}^{3-}$.

The high field center, reported by Zeldes and Livingston also fall into the same category. Measurements give

High field center (T∼77°K)

	g_{xx}	g_{yy}	g_{zz}
	1.6334	1.5716	1.8482
θ	96.4°	89.5°	6.2°
φ	31.0°	36.9°	26.4°

These centers are produced by gamma irradiation, but are not stable at room temperature, in contrast to the vacuum reduction centers. Gamma irradiations are carried out at 77°K, and observations also made at this temperature. More recently Mason, Koehler, and Kikuchi[20] have shown that thermoluminescent peak at 225°K, trap depth 0.55 ev, is to be identified with this high-field center.

VIII. THERMOLUMINESCENCE AND ESR

When a crystal of CaWO$_4$ is slowly warmed after gamma irradiation at 77°K, bursts of visible radiations are emitted. For a "pure" CaWO$_4$, the so-called
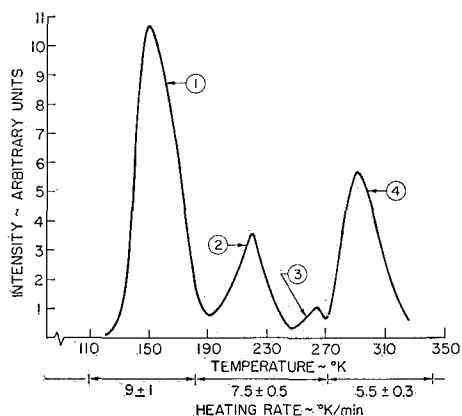

Fig. 21. Glow curve for a nominally pure CaWO$_4$ following 300 kilorad gamma irradiation at 78°K. The peaks 1 (at 155°K), 2 (at 225°K), and 4 (at 290°K) are to be identified with ESR lines A, B, and C in Fig. 22.

(30)

glow curve is as shown in Fig. 21. The peaks occur at 155°, 225°, and the associated trap depths are 0.36, 0.55, and 0.72 ev, respectively.

To identify the traps, the effect of successive warming of the sample upon the ESR spectrum was investigated. Immediately after irradiation at 77°K, the ESR spectrum consists of groups of lines, which can be identified with paramagnetic Nb^{4+}, as discussed earlier, and two tungsten centers, A and B, as shown in Fig. 22. The line A can be readily shown to be the same as the low-field
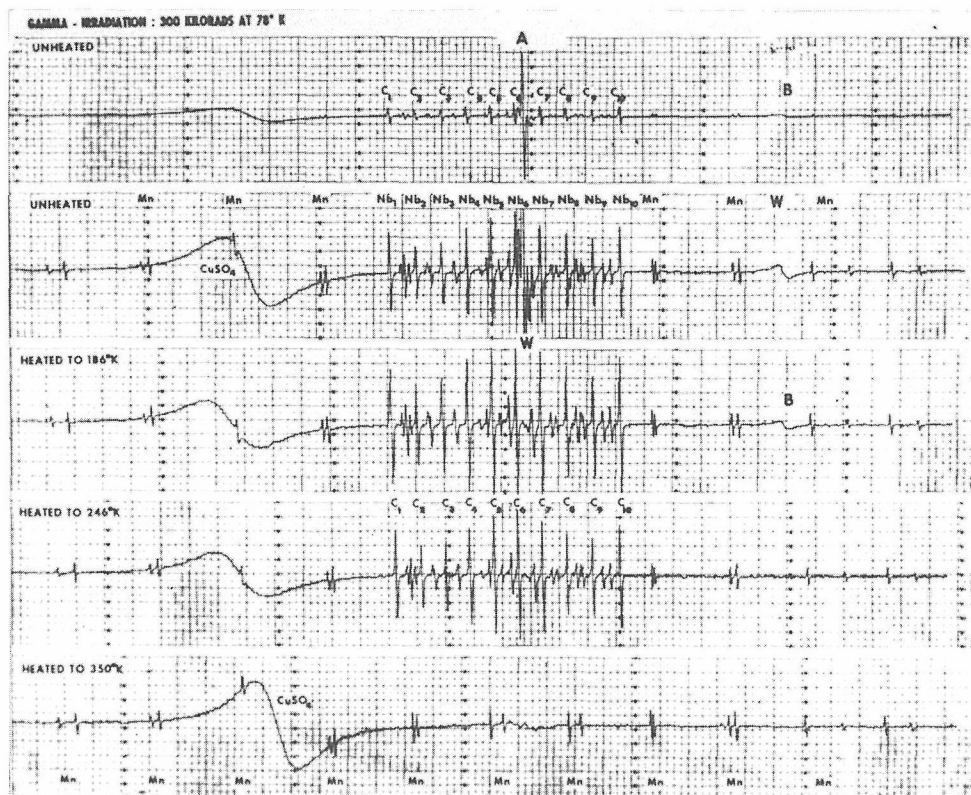

Fig. 22. Effect of sample warming upon ESR spectra. Note that the lines A (W_A-center), B (W_B-center), and C (Nb-center) disappear when the sample is warmed to 186°, 246°, and 350°K respectively.

center reported by Zeldes and Livingston, and the line B is seen to be very close, if not identical, to the high-field W-line reported by the same workers. Aside from a small difference in the g-value along the c-axis, which may or may not be real, there appears to be a slight difference in the temperature dependence of the line width. The Oak Ridge workers reported the marked temperature dependence but were able to make the identification at liquid nitrogen temperature. For the sample investigated in our laboratory, the line B is still very broad at 77°K, so that much lower temperatures are required to reveal the satellite structure. This difference, however perhaps is to be expected because the high-field B-center is sensitive to nearby impurities and defects, as we have seen. The third trace in Fig. 22 shows that the A-line disappears after the sample has been

heated to 186°K, showing therefore that the low-temperature 155°K thermoluminescence peak is to be associated with the low field paramagnetic W-center. As indicated earlier, this center has been assigned to WO_4^-. From the fourth trace, we note that the B-line disappears after warming to 246°K so that this thermoluminescence peak arises from electrons being released from WO_4^{3-} centers, and finally the 290°K is associated with the release of holes from the NbO_4^{2-} centers.

Additional evidence that the 225°K peak arises from the WO_4^{3-} traps is provided by the glow curves of rare-earth doped $CaWO_4$ samples. Figure 23 gives the glow curves for nominally pure $CaWO_4$ sample doped with 1% Sm, and another containing about 0.5% Tb. We note that the 155°K peak is conspicuously absent in the rare-earth doped samples and a marked increase in the intensity of the 225°K peak. Evidently the trivalent rare-earths such as Sm^{3+} and Tb^{3+}, have the effect of stabilizing the WO_4^{3-} centers.
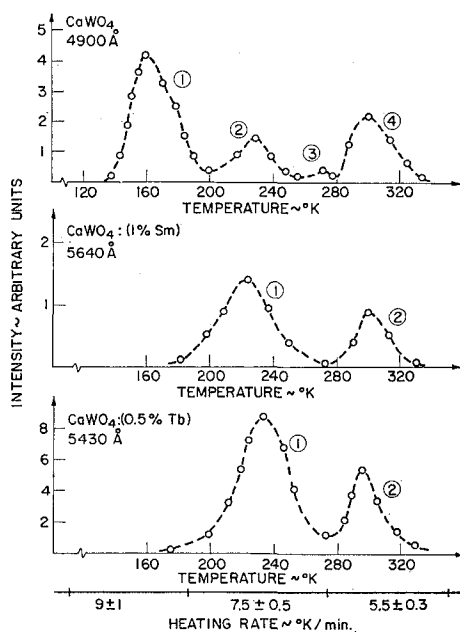
Fig. 23. Glow curves of $CaWO_4$ samples doped with Sm and Tb. Note that the 155°K thermoluminescence peak (W_A-center) is missing for the Sm and Tb samples.

VIII. FAST NEUTRON DAMAGE CENTERS

So far we have been concerned with the effect of gamma rays. The mechanisms involved are the photoelectric and Compton effects, which upon displacing electrons lead to the production of electron deficient and electron excess paramagnetic centers. Effectively only electron displacements need be taken into account because gamma photon linear momentum is small. We next focus our attention on fast neutrons which can produce atomic displacements and hence lead to possibly more complex paramagnetic centers. The problem to be discussed[21] is interesting for two reasons, namely (1) certain defect centers can be

positively indentified and (2) the defect concentration is in good agreement with the Kinchin-Pease theory.

The effect of fast neutron irradiation upon the ESR spectrum of nominally pure $CaWO_4$ single crystal is shown in Fig. 24. The spectrum was taken with the magnetic field along the crystal c-axis at 77°K. The lower trace, taken before irradiation, shows that the sample contained about 10^{16} Mn atoms per gram of the sample. The upper trace was taken after the sample had been in the Phoenix Laboratory 2 MW swimming-pool type reactor for several hours. There are three groups of lines, which have been labeled α, β, and γ. These lines are not produced by room temperature x or gamma-irradiation, their intensities are not reduced upon cadmium shielding, and furthermore the ESR lines can be annealed out by heating the sample at 600°C for about an hour. Thus the centers are associated with atomic vacancies.
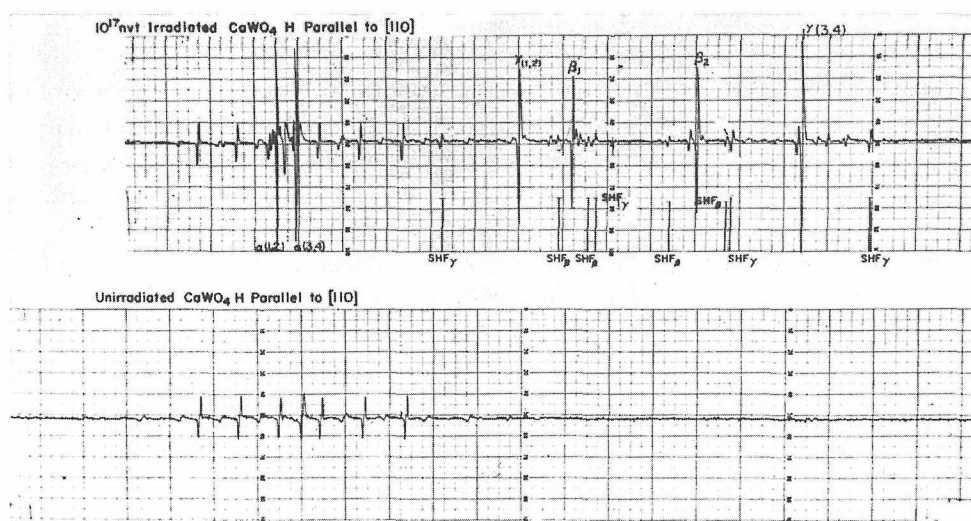

Fig. 24. ESR spectrum of fast neutron irradiated $CaWO_4$ crystal. The neutron dose is about 10^{17} nvt. The spectrum is taken at 78°K with magnetic field along the c-axis.

The identity of the α-group is not known, but both the β- and γ-groups are paramagnetic tungsten centers stable at room temperature or above. A careful examination of the strong lines shows that each is accompanied by a pair of weak satillites whose intensities are about 1/12 of the central component. Moreover, during irradiation the sample is placed near the reactor core, where the temperature is about 60°C and after irradiation pulled to the side and left in the reactor pool for a few days to allow the induced radioactivity to decay out.

Study of the angular dependence of the ESR spectra suggests and the β- and γ-centers are paramagnetic W associated with Ca and O vacancies respectively. To see this, consider the plot of the γ-center ESR spectra shown in Fig. 25. The plot is obtained by varying the magnetic field in a plane containing the face diagonal of the tungstate radical (see insert). Since any one of the 4 oxygens can be displaced, there will in general be four magnetically inequivalent W's but of the magnetic field is in the face-diagonal plane, two of the W's, as-
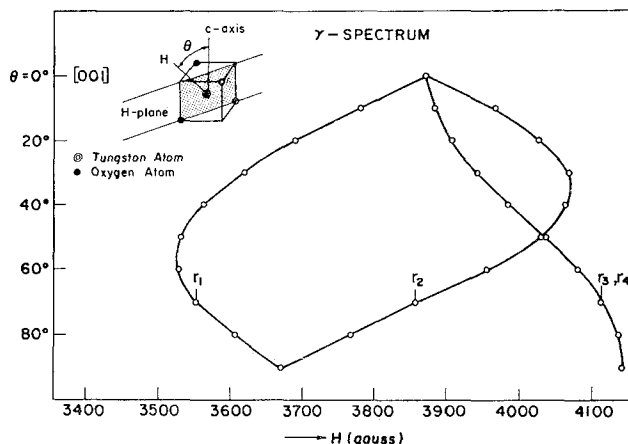
Fig. 25. Angular dependence of γ-center ESR spectrum.

sociated with vacancies at A, B will be equivalent, so that the ESR spectrum is expected to consist of three lines, one of which having the twice the intensity of the other. However, if the magnetic field is along the c-axis, all four sites become equivalent, and if in the ab- plane, sites C and D because equivalent. It will be noted that the ESR spectrum does show the expected symmetry.

This model also suggests that one of the g- tensor principal axes is along the broken W-O bond direction and that another one is in the ab plane. The unpaired spin results from the breaking of a W-O bond so that the charge density of the unpaired electron can be expected to be almost, if not entirely, along this direction. Crystal structure data indicate that the W-O bond direction is given by the angles $\theta=56°44'$ and $\varphi=31°54'$. Measurements show that the major principal axis with $g_{zz}=1.914$ makes $\theta=57°$ with the c-axis and $\varphi=32°$ with the a-axis. Furthermore, the oxygens on the tungstate are located on the alternate corners of a slightly squashed tetrahedron (square base of 2.11 A and height 1.96 A), so that the three oxygens still bonded to the W form an isoseles triangle, with the base in the ab plane. Consequently, one of the principal axis direction is expected to be in the ab-plane, but because of the very small distortion, the two g-values are expected to be very nearly the same. This is in fact confirmed by measurements; the values are 1.675 and 1.646 respectively.

The concentration of γ-centers was established by comparing with a known weight of copper sulfate standard. The samples of copper sulfate and calcium tungstate were 1.52 mg and 270 mg respectively. The $CaWO_4$ was irradiated for an hour in the reactor. In this manner, it was found that the number of γ-center is 1.29×10^{16} spins. Since each oxygen vacancy is expected to give rise to a single unpaired spin, the measured oxygen vacancy in the sample is also the same, giving the concentration

$$1.29 \times 10^{16}\left(\frac{6.06}{0.27}\right) = 2.57 \times 10^{17}/\text{cm}^3.$$

To estimate the defect concentration we use the well known results

$$n_p = (\phi t) n_0 \sigma_d$$

$$n_d = n_p \bar{\nu}$$

in which n_p is the concentration of primary knock-ons, (ϕt) is the integrated fast flux, n_0 is the density of scattering centers in the target material, σ_d is the displacement cross-section, n_d is the vacancy concentration, and $\bar{\nu}$ is the average number of atomic displacements per primary knock-on.

Furthermore, we assume that there exists a sharp ionization limit E_c, above which the moving charged particle loses energy by ionization but below which the energy is lost by "hard sphere" collisions with other lattice atoms. The number of atomic desplacements for a primary knock-on can be shown to be

$$\bar{\nu} = \frac{E_c}{2E_d} \qquad \text{if} \quad E_p > E_c,$$

$$\bar{\nu} = \frac{E_p}{2E_d} \qquad \text{if} \quad E_p < E_c,$$

in which E_p is the primary knock-on recoil energy, given by

$$E_d = \frac{1}{2} \Gamma_m = \frac{2mM}{(M+m)^2} E_0 \sim \frac{2E_0}{A}.$$

Using $E_0 = 2$ MeV, as the average energy of fission reactor neutrons, we obtain

$$E_p = \frac{4}{A} \quad (\text{MeV}).$$

For the displacement cross-section, σ_d, we note

$$\sigma_d = \sigma_{0c}\left(1 - \frac{E_d}{T_m}\right) \sim \sigma_{0c},$$

since the displacement threshold energy is small in comparison to the maximum primary knock-on recoil energy. The displacement cross-section then are just the scattering cross-sections that can be found from such sources as the "Barn Book".

During the irradiation period of 1 hour, the flux was found to be about 1×10^{12} n/cm^2/sec, so that

$$(\phi t) = 1.36 \times 10^{16} \text{ n/cm}^2.$$

Hence we find that

	n_0 ($\times 10^{22}$)	σ_{sc} ($\times 10^{24}$)	n_p ($\times 10^{15}$)
O	5.08	3	.55
Ca	1.77	3	.14
W	1.27	10	.49

Furthermore, for the primary knock-on energy, limiting energy of ionization E_c, and the displacements per primary knock-on, we obtain

	E_p (kev)	E_e (kev)	$\bar{\nu}$	n_d ($\times 10^{17}$)
O	250	16	320	1.8
Ca	100	40	800	1.1
W	21.7	184	434	2.0

The total concentration of vacancies is then about

$$3.3 \times 10^{17}/\text{cm}^3.$$

Of which the oxygen vacancy concentration is about

$$2.9 \times 10^{17}/\text{cm}^3.$$

This is in very good agreement with the ESR measurements.

Samples used in these studies were prepared by placing in polyethylene bottles weighted down by bismuth slugs and then irradiated in the Phoenix Memorial Laboratory Swimming-pool type reactor. To maximize the fast neutron flux, the bottles were placed close to the reactor core where the temperature is approximately 60°C. The irradiation times varied from 20 minutes to 20 hours. Longer irradiations were not feasible because of the excessive induced radioactivity, coming from ^{185}W and ^{187}W. Furthermore to minimize induced radioactivity, tha samples were wrapped in 30 mil cadmium sheets formed into a cylinder. After irradiation the samples were moved to the side of the reactor pool, to permit the radioactivity to die out. This period varied from three to fifteen days, depending upon the irradiation dose.

For these reasons, the W centers studied here are stable up to at least 60°C, with lifetimes of more than a few days. Low temperature neutron irradiation may possible yield other W centers. Furthermore gamma irradiation may produce other W centers.

IX. DISCUSSION

Upon inspecting the list of metastable ESR centers in $CaWO_4$, we note that for some, $g > g_e$ and for others $g < g_e$. We shall refer to those in the first category as the "A" group. The examples are[22,23]

	g_{001}	g_{110}
V	2.024	2.037
Nb	2.022	2.026
Ta	2.019	
W_A^{5+}	2.009	2.0179

The first three of course are elements in Group V of the Periodic Table, and the last is the low-field paramagnetic W-center and is responsible for the glow curve peak at 155°K. There are possibly many other centers in this group. For example G. H. Azarbayejani reports that upon x-irradiation at 78°K of samples containing Y and La, centers with $g > 2$ are produced. P. R. Edwards et al.[24,25]

have reported centers due to PO_4^{2-} and AsO_4^{2-}; these may also fall into group "A". It would also be of interest to investigate the effects of x- or gamma-irradiation upon neutron irradiated samples.

The centers for which $g < g_e$ can be put into several groups. First there are the centers due to the Group VI elements, namely

	$g_{//}$	$g_{\perp}$
Cr	1.988	1.943
Mo	1.987	1.887
W	1.850	1.60

In a sense these are not centers of direct concern to us, but have been included because they assist in the assignment of the centers; as it will be recalled the centers are assigned to CrO_4^{3-}, MoO_4^{3-}, and WO_4^{3-}.

There are several WO_4^{3-} centers, which we shall, for sake of brevity, refer to as W_B centers.

W_B Centers

g_{33}	g_{11}	g_{22}	Stabilizer
1.8491	1.6048	1.5726	Y
1.71419	1.66303	1.53096	La
1.8482	1.6334	1.5716	(?)

The first two have been reported to this author by G. H. Azarbayejani.[9] The last is the high-field center reported first by H. Zeldes and R. Livingston.[18] These results suggest that the W_B-centers are sensitive to the charge stabilizer and suggest the need of investigating other W_B centers stabilized by other trivalent rare-earths. The effects of Sm and Tb upon the glow curve have been noted; however the complementary ESR studies have not been carried out. The characteristics of these centers are that the g-values fall approximately in the same range, the major g-tensor principal axis is almost along the c-axis, and the remaining two g-values do not differ appreciably from each other.

It is tempting to include the β-center produced by fast neutrons in this group. But the g-values 1.801, 1.791, and 1.724 giving $\langle g \rangle = 1.772$ seem to be somewhat larger than those of W_B. Furthermore, if this center is associated with a Ca-vacancy, the mechanism responsible for the stabilization of the center becomes uncertain. In any case, further systematic studies are needed. Particularly a search should be undertaken for other tungsten centers produced by gamma-irradiation of neutron irradiated samples at low temperatures.

Also these investigations indicate clearly the potential usefulness of irradiation and ESR as a tool for chemical analysis. It will be recalled that Nb was detected even in the so-called pure $CaWO_4$ crystal.

ACKNOWLEDGEMENTS

REFERENCES

(1) C. Kikuchi, S. Yip., S. H. Chen. "Applications of Spin Resonance Techniques to the Study of Radiation Effects," Michigan Memorial Phoenix Project report based on lectures given at the Neutron Physics Conference, Mackinac Island, Mich., June 12–17, 1961.

(2) For the various references, see S. A. Marshall and J. A. McMillan, "Electron Spin Resonance Absorption Spectrum of CO_2- Molecule Ions Associated with F-Ions in Single-Crystal Calcite," *J. Chem. Phys.*, 49, 4887 (1 Dec. 1968).

(3) N. Itoh and M. Saidoh "Radiation-Induced Interstitial Centers in Alkali Halides," *Phys. Stat. Sol.*, 33, 649 (1969).

(4) L. F. Johnson and K. Nassau, *Proc. IRE*, 49, 1704 (1961); also see L. F. Johnson, *Quantum Electronics*, Paris, Vol. II, 1963, p. 1021.

(5) K. Nassau, "The Theory of Coupled Substitution", *Phys. Chem. Solids*, 24, 1551 (1961).

(6) G. B. Beard, W. H. Kelley, and M. L. Mallory, "Temperature Dependent Luminescence of $CaWO_4$ and $CdWO_4$," *J. Appl. Phys.*, 33, 144 (Jan. 1962).

(7) M. Sayer and W. R. Hardy, "Scintillation Decay in Calcium Tungstate," *Can. J. Phys.*, 43, 1925 (1965).

(8) K. Nassau and A. M. Broyer, "Calcium Tungstate: Czochralski Growth, Perfection, and Substitution," *J. Appl. Phys.*, 33, 3064 (Oct. 1962).

(9) G. H. Azarbayejani, Private Communication.

(10) See, for example, P. W. Atkins and M. C. R. Symons, "The Structure of Inorganic Radicals," (Elsevier, Amsterdam, 1967).

(11) D. S. Schonland, "Electron Resonance Studies of Transition Metal Oxyions. II. Theory of Electron Resonance in Manganate," *Proc. Roy. Soc.*, A254, 111 (1960).

(12) E. Banks, M. Greenblatt, and B. R. McGarvey, "ESR and Optical Spectroscopy of CrO_4^{3-} in Chlorospodiosite, Ca_2PO_4Cl," *J. Chem. Phys.*, 47, 3772 (15 Nov. 1967).

(13) A. Zalkin and D. H. Templeton, "X-Ray Diffraction Refinement of the $CaWO_4$ Structure," *J. Chem. Phys.* 40, 501 (1964).

(14) M. I. Kay, B. C. Frazer, and I. Almodovar, "Neutron Diffraction Refinement of $CaWO_4$," *J. Chem. Phys.*, 40, 504 (15 Jan. 1964).

(15) K. V. Lingman, P. G. Nair, and B. Venkataraman, "Electron Spin Resonance of Cr^{5+} in $CaWO_4$."

(16) G. H. Azarbayejani and A. L. Merlo, "Electron Spin Resonance of Mo^{5+} in $CaWO_4$," *Phys. Rev.*, 137, A489 (18 Jan. 1965).

(17) K. C. Chu and C. Kikuchi, "Paramagnetic Centers in Neutron Inodiated Calcium Tungstate Single Crystals," *IEEE. Trans.*, NS-13, No. 6, 41 (Dec. 1966).

(18) H. Zeldes and R. Livingston, "Paramagnetic Resonance Study of Irradiated Single Crystals of Calcium Tungstate," *J. Chem. Phys.*, 34, 247 (1961).

(19) K. C. Chu, C. Kikuchi, and W. Viehmann, "ESR of Niobium in $CaWO_4$," *J. Chem. Phys.*, 46, 386 (1 Jan. 1967).

(20) D. R. Mason, H. A. Koehler, and C. Kikuchi, "Identification of Defect Sites in $CaWO_4$ from the Correlation of ESR and Thermoluminescence Measurements," *Phys. Rev. Letters*, 20, 451 (26 Feb. 1968).

(21) K. C. Chu and C. Kikuchi, ,,Direct Measurement of the Oxygen Vacancies Produced

Calcium Tungstate by Fast Reactor Neutrons," *Phys. Rev.*, **169**, 752 (15 May 1968).

(21) N. Mahootian, C. Kikuchi, and W. Viehmann, "Spin Resonance Properties of Scheelites. I. Vanadium in $CaWO_4$," *J. Chem. Phys.*, 48, 1097 (1 Feb. 1968).

(23) S. R. Irizarry-Milan, D. Mason, and C. Kikuchi, "EPR of Ta in $CaWO_4$," *Bull. Am. Phys. Soc.*, 14, 599 (1969).

(24) P. R. Edwards, S. Sabramanian, and M. C. R. Symons, "Electron Spin Resonance Studies of Vanadate, Niobate, Phosphate, and Arsenate in γ-irradiated Calcium Molybdate and Calcium Tungstate," *Chem. Comm.*, 799 (1968).

(25) P. R. Edwards, S. Subramanian, and M. C. R. Symons, "Structure and Reactivity of the Oxyanions of Transition Metals. Part XVII, A study of NbO_4^{2-} in Calcium Molybdate by Electron Spin Resonance," *J. Chem. Soc.*, (A) 2985 (1968).

(26) G. K. Born, R. J. Grasser, and A. O. Scharmann, "EPR and Thermoluminescence Measurements on $CaWO_4$ Crystals," *Phys. Stat. Solidi*, 28, 583 (1968).

(27) P. Bräunlich, K. Reiber, and A. Scharmann, "Luminescence and Condictivity Investigations of Single Crystal $CaWO_4$," *Zs. of Physik*, 183, 431 (1965).

(28) H. A. Koehler, C. Kikuchi, and D. Mason, "Paramagnetic Thermoluminescent Centers in $CaWO_4$," *Physica Stat. Solidi*, 31 (1969).

(29) C. Kikuchi and D. L. Tseng, "EPR and ENDOR of Nb^{4-} in $CaWO_4$," *Bull. Am. Phys. Soc.*, 14, 188 (1969).